ARTICLE   OPEN

Check for updates

The role of sea surface temperature in shaping the characteristics of future convective afternoon rainfall in Taiwan

Wan-Ru Huang [1] ✉, Yu-Tang Chien [1,2], Chao-Tzuen Cheng [2], Huang-Hsiung Hsu [3] and Suranjith Bandara Koralegedara [1]

Convective afternoon rainfall (CAR) is a significant summer rainfall feature in Taiwan. This study investigates the projected uncertainties in summer CAR in Taiwan, using a dynamical downscaling approach with the Weather Research and Forecasting Model (WRF) and the High-Resolution Atmospheric Model (HiRAM). The projections were driven by four different sea surface temperature (SST) categories derived from CMIP5 model simulations under the RCP8.5 scenario. All projections indicate a reduced frequency but increased intensity of CAR over Taiwan by the end of the 21st century. However, notable differences in the degree of CAR changes were observed among simulations with varying degrees of Pacific SST warming. These variations in potential future changes in CAR frequency and intensity can be attributed to the variations in daytime thermal instability, local inland wind convergence, and moisture flux convergence over Taiwan. Furthermore, this study explored the linkage between local thermodynamic conditions and projected large-scale circulation patterns.

INTRODUCTION

Diurnal rainfall is a common phenomenon in coastal regions and oceanic islands worldwide[1–5], including Taiwan. Numerous observational and modeling studies have demonstrated the diversity of diurnal rainfall characteristics over the East–Asian monsoon region[4,6–12]. In Taiwan, diurnal rainfall during summer (June, July, and August; JJA) generally occurs in the late afternoon, with the rainfall peak typically observed between 14:00 and 17:00 local standard time (LST)[13]. These diurnal rainfall events are also commonly referred to as convective afternoon rainfall (CAR) events due to their timing with prevalent convection. Previous studies on Taiwan rainfall data have revealed that CAR events dominate the summer rainfall, accounting for over 40 ~ 50% of the total summer rainfall[14,15]. Therefore, understanding the underlying physical mechanisms influencing CAR event characteristics is crucial to improving the accuracy of CAR events projection in Taiwan[16].

Both observational and modeling approaches have been employed to investigate the impact of climate on CAR features in Taiwan[13,17,18]. Observational studies have demonstrated variations in CAR frequency and intensity at multiple timescales, including long-term trends and interannual variability[17,19]. For instance, Huang et al.[19] analyzed rain gauge observations from 1961 to 2012 to examine the CAR features over Taiwan and identified a declining trend in CAR frequency but an increasing trend in intensity. These trends were attributed to local and large-scale atmospheric thermodynamic changes, such as a decreased daytime wind convergence, increased thermal stability, and enhanced moisture supply over Taiwan. In addition, the studies employing climate models[18] or dynamical downscaling models[13] projected future changes in CAR events over Taiwan, indicating a decrease in the frequency but an increase in the intensity of CAR events by the end of the 21st century. These future changes in CAR characteristics over Taiwan[13,18] were also linked to the

anticipated changes in multiple-scale atmospheric thermodynamic factors, consistent with the findings of Huang et al.[19]. However, the future projection examined by Huang et al.[13,18] did not consider the uncertainties of future SST projection, which may affect the CAR activity over Taiwan.

Many studies have utilized global climate models to project the effects of global warming on future rainfall distributions[20–23]. For instance, Mizuta et al.[20] categorized future changes in global SST distribution into four distinct categories, based on their analysis of 28 models from the Coupled Model Intercomparison Project Phase 5 (CMIP5)[24]. They discovered that the impact of variations in SST warming patterns could contribute to the reduced consensus among CMIP5 models when predicting changes in regional rainfall and atmospheric circulation. Chen et al.[25,26] followed Mizuta et al.[20] and examined different SST impacts over the western North Pacific and East Asian rainy seasons, emphasizing the general circulation patterns and associated daily rainfall characteristics. In contrast to the studies mentioned above, which either primarily concentrated on larger-scale features[20,25,26] or employed a single SST forcing for simulating future changes in CAR activities[13,18], this research aims to provide valuable insights into how projections regarding CAR activities in Taiwan may change in the future in response to the four types of SST warming patterns classified by Mizuta et al.[20].

Some indications for the role of the SST changes in affecting the CAR activity over Taiwan have been examined by Huang et al.[17], using observational data during the summer of 1960−2012. It was demonstrated that when the SST over the domain of 5°N−5°S and 170°W−120°W (herein NINO3.4 index) is cooler (warmer), CAR occurred more (less) frequently in Taiwan, indicating the influence of El Niño Southern Oscillation (ENSO) on local weather. However, the relationship between CAR intensity and the NINO3.4 index shifted from positive to negative around the mid-1980s due to changes in local moisture flux convergence over Taiwan in

[1]Department of Earth Sciences, National Taiwan Normal University, Taipei, Taiwan. [2]National Science and Technology Center for Disaster Reduction, New Taipei City, Taiwan. [3]Research Center for Environmental Changes, Academia Sinica, Taipei, Taiwan. ✉email: wrhuang@ntnu.edu.tw
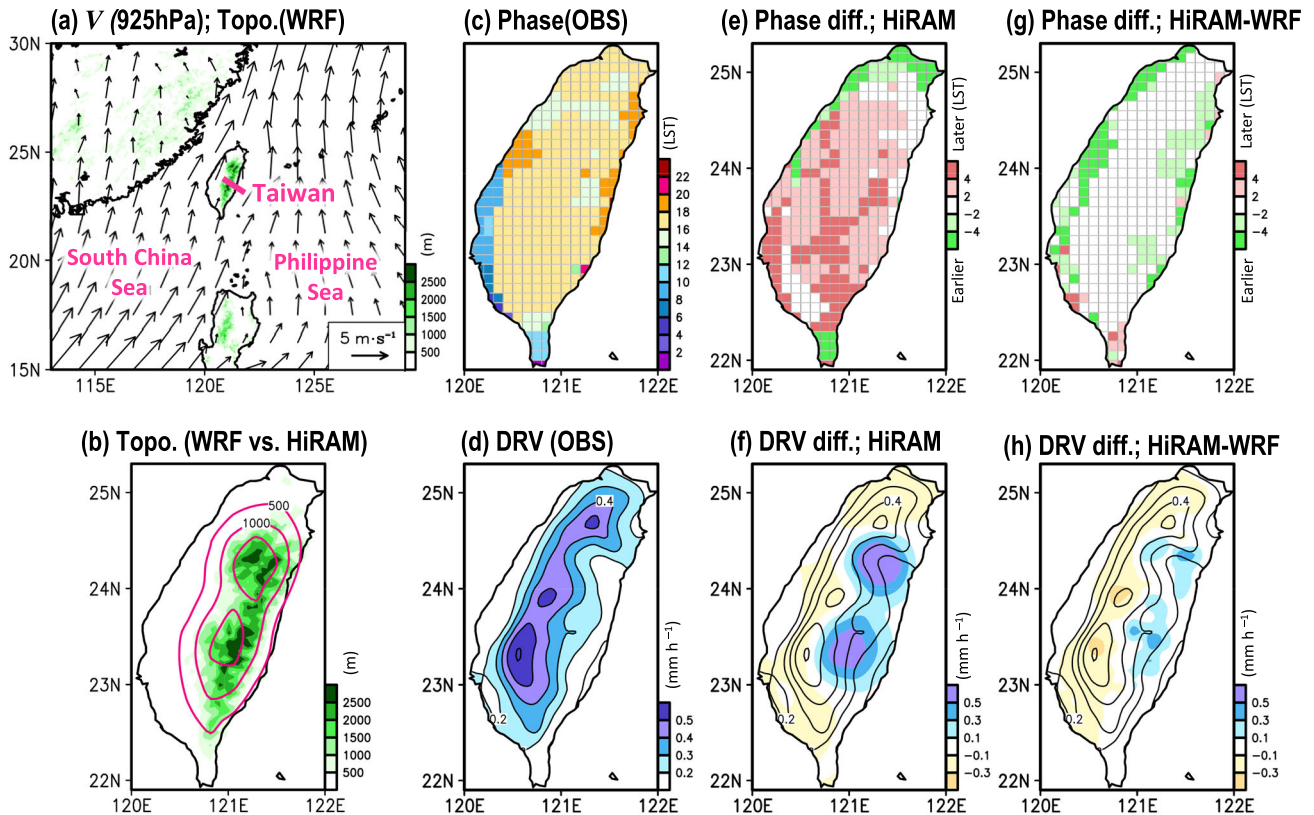
Fig. 1 Verification of model's performance in rainfall simulation. a The domain used in the HiRAM-WRF model simulations superimposed with the topography (shaded) and the 925 hPa wind circulation (vectors). The locations of Taiwan and the surrounding important seas are indicated. **b** A zoomed-in map of Taiwan depicting the topography used in the WRF model (shaded) in comparison with those used in the HiRAM (line contours; 500 m interval). **c** Peak timing phase of the diurnal evolution of rainfall estimated from gridded rain-gauge observations (OBS) in the local standard time (LST). **d** Diurnal rainfall variability (DRV) estimated from OBS (see Eq. (1) for the calculation method). **e** Difference between the diurnal rainfall peak timing phase estimated from HiRAM and OBS. **f** Difference between the DRV of HiRAM and OBS (shaded) superimposed with the DRV of OBS (contoured). **g**, **h** are similar to (**e**, **f**) but for the related differences between HiRAM-WRF and OBS.

response to the SST variations over the NINO3.4 region. Based on these observations, it is plausible to expect that different types of future SST changes may impact the CAR features in Taiwan differently; this study is motivated to explore this issue.

The main objective of this study is to address two key questions: (1) How will the characteristics of CAR events in Taiwan change under the influence of different SST future projection patterns? (2) Do the observed changes in question (1) above, indicate the influence of ENSO on future local CAR variations? By exploring these questions, we also aim to demonstrate whether the previously observed impact of ENSO on CAR activities in Taiwan[17] remains valid in future projections. This paper builds on the results of higher-resolution simulations and future climate projections under Representative Concentration Pathways 8.5 (RCP8.5) scenario[27], where we adopted a dynamical downscaling approach, using the Weather Research and Forecasting model (WRF)[28,29] simulations driven by output from the High-Resolution Atmospheric Model (HiRAM)[30]. Compared to the resolution of HiRAM (~25 km), its related dynamical downscaling with the WRF model (hereafter HiRAM-WRF) has a finer resolution (~5 km). It is important to note that a cumulus parameterization was not used in HiRAM-WRF simulations, based on prior findings that suggest a closer alignment of rainfall simulation with observed patterns at finer resolutions[31–33]. For the sensitivity testing of the impact of potential future SST changes, the four SST categories proposed by Mizuta et al.[20] were used as the boundary conditions for both HiRAM and HiRAM-WRF simulations. All analyses were focused on the climate average for the past (1979−2003) and future (2075−2099) JJA periods.

RESULTS

CAR features: simulation and projection

Prior to the detailed examinations, we demonstrated that HiRAM-WRF has an improved capability in simulating the diurnal rainfall feature in Taiwan compared to HiRAM. The domain of HiRAM-WRF covers the East Asian summer monsoon region (Fig. 1a). When compared to HiRAM, HiRAM-WRF integrates high-resolution topography data, enabling a more accurate representation of the terrain variations in Taiwan (Fig. 1b). By examining the timing of the maximum hourly rainfall for each grid point from ground observations (hereafter OBS) (Fig. 1c), we observed that the peak timing typically occurs in the late afternoon for most areas of Taiwan, except the coastal regions. The spatial distribution of diurnal rainfall variability (DRV) estimated from OBS (Fig. 1d) further shows that the region located along the west of the central mountain range exhibits a larger variability than the other sub-regions. Comparing these temporal and spatial observed features with the simulation results from HiRAM (Fig. 1e–f), we noted that: (1) HiRAM tends to simulate the diurnal rainfall peak later than the OBS peak over the area with larger observed DRV (Fig. 1e), and (2) the DRV difference between HiRAM and OBS (shaded in Fig. 1f) shows that HiRAM has two larger hotspots of DRV difference compared to OBS over the central mountains in Taiwan, reflecting errors in simulating diurnal rainfall in mountainous regions. Relative to HiRAM, the HiRAM-WRF tends to simulate diurnal rainfall with a peak timing closer to OBS over a larger domain of Taiwan (Fig. 1g). Regarding the spatial distribution of DRV, while HiRAM-WRF also exhibits differences when compared to OBS, these differences (shaded in Fig. 1h) are relatively less pronounced
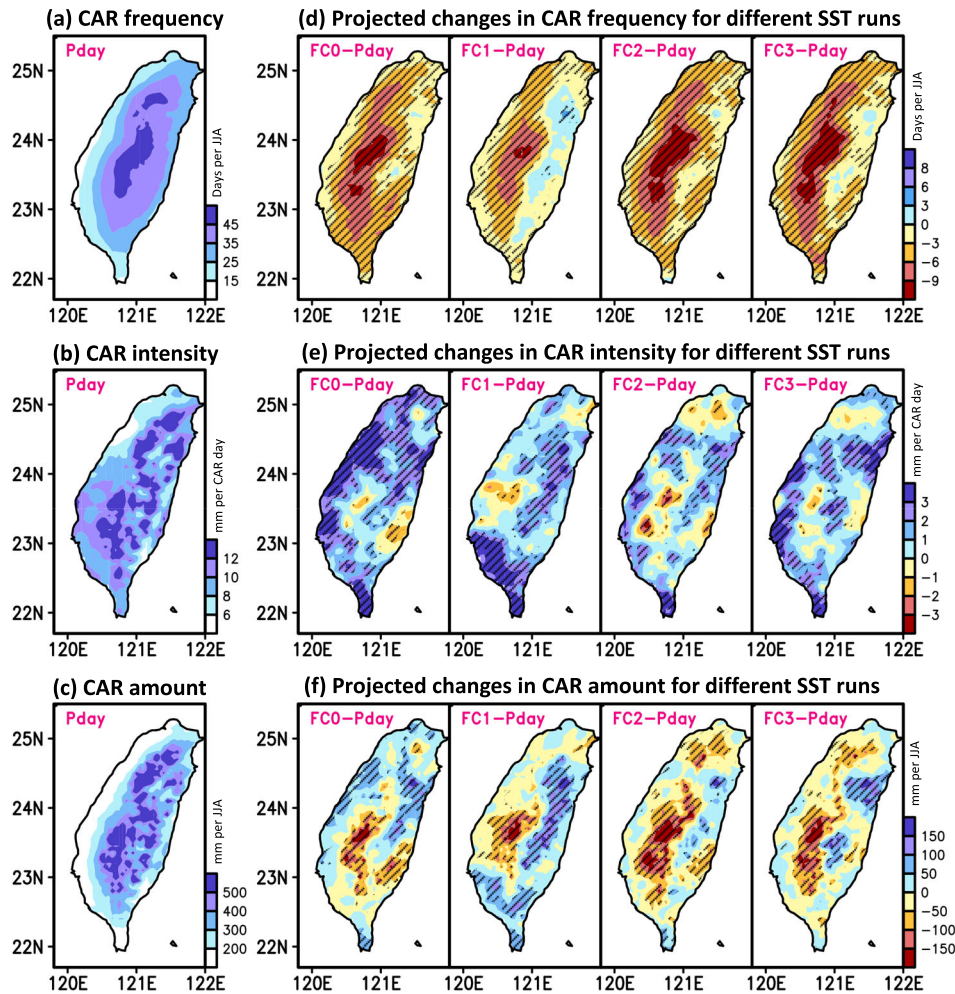
Fig. 2 Present and future CAR characteristics in HiRAM-WRF simulations. Present-day (Pday) simulations of (**a**) CAR frequency, (**b**) CAR intensity, and (**c**) CAR amount averaged during 1979–2003 JJA. **d**–**f** is related to (**a**–**c**) respectively, but for the future projected changes (future minus Pday) in four future runs for the different sensitivity testing of SST (hereafter FC0, FC1, FC2, and FC3). All future runs are estimated from the average of 2075–2099 JJAs. The black hatched area represents the significant changes at the 90% confidence interval in (**d**–**f**).

and are scattered over smaller spatial extents compared to HiRAM (shaded in Fig. 1f). Furthermore, we note from Supplementary Fig. 1 that the distribution of observed CAR amount and the model errors in reproducing the CAR amount demonstrate similar findings to the DRV features mentioned above. Nevertheless, it should be noted that compared to OBS, both HiRAM and HiRAM-WRF tend to overestimate CAR amount in the mountainous region and underestimate CAR amount in the west of the mountains. Despite these model errors, overall, the results in Fig. 1 and Supplementary Fig. 1 highlight that the simulated DRV and related CAR events in HiRAM-WRF are closer to the OBS in terms of temporal and spatial distribution. Based on the above validation, we mainly focused on the results of HiRAM-WRF in simulating and projecting the local rainfall features in Taiwan.

Next, we construct the rainfall frequency (Fig. 2a), rainfall intensity (Fig. 2b), and rainfall amount (Fig. 2c) identified from the average of CAR events during 1979−2003 JJAs, simulated by HiRAM-WRF. Overall, the present-day (hereafter Pday) simulations using HiRAM-WRF show that (1) CAR is more frequent along the west side of the mountain areas; (2) CAR is also more intense over the mountain areas, but its spatial distribution is more scattered than those observed in frequency distribution; (3) the spatial distribution of CAR amount is a mixed feature with a larger value along the west side of mountain areas similar to the pattern seen in CAR frequency, but also some maximum values over the east

side of the mountain similar to the results of CAR intensity. These spatial patterns revealed in Fig. 2a–c are consistent with earlier studies[13,34] that focused on a shorter study period (1994−2003), supporting the robustness of our analysis methods in identifying the CAR events in HiRAM-WRF.

In this study, we analyzed the future simulations using the four different sets of SST forcing data from Mizuta et al.[20] (hereafter FC0, FC1, FC2, and FC3 or all future runs for short). Mizuta et al.[20] classified the normalized SST changes between the future and the Pday from 28 CMIP5 models into four categories (see Supplementary Table 1 for the 28 models and Supplementary Table 2 for the classification procedure). As indicated in Supplementary Table 1, the SST patterns of FC0, FC1, FC2, and FC3 are based on the multi-model ensemble mean of 28, 8, 14, and 6 CMIP5 models, respectively. It's important to note that all these categories (FC0–FC3) represent potential future scenarios within the CMIP5 framework. Earlier modeling studies[13,18], which did not consider the sensitivity testing of SST forcing, have demonstrated that the CAR events in Taiwan will become less frequent but more intense in the future compared to the present. Moving a step forward from this finding, we demonstrated that all four future runs for the sensitivity testing of SST suggest a decrease in CAR frequency (Fig. 2d) and an increase in CAR intensity (Fig. 2e) over most of Taiwan. This result reflects that the "sign" (positive or negative) of projected changes in area-averaged CAR frequency and intensity

(a) CAR frequency diff. (b) CAR intensity diff. (c) CAR amount diff.
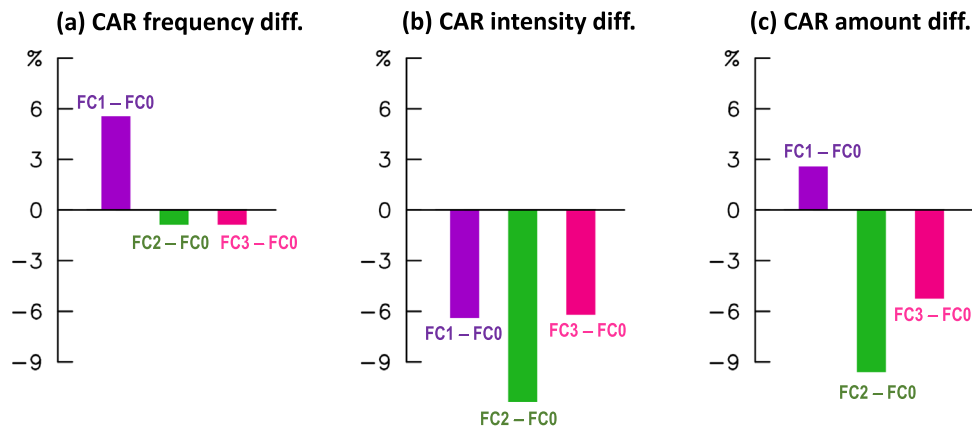
Fig. 3 Differences in projected changes of CAR characteristics. HiRAM-WRF's simulations of percentage differences in the area-averaged CAR activities over Taiwan: (**a**) CAR frequency, (**b**) CAR intensity, and (**c**) CAR amount. The values of percentage for each run (FC0, FC1, FC2, and FC3) are estimated from Eq. (3), while the differences in percentage are estimated from the differences between the future projection using the FC0 run and the other three future runs (denoted as FC1 − FC0 (purple bar), FC2 − FC0 (green bar), and FC3 − FC0 (pink bar)).

is not very sensitive to the SST changes (Supplementary Table 3). Regarding the spatial characteristics, all future runs show that the decrease in CAR frequency is most significant along the windward side of the southwesterly prevailing wind (Figs. 1a and 2d). Huang et al.[13] examined the possible causes of a larger decrease in CAR frequency over western Taiwan than over eastern Taiwan and suggested this east-west difference is attributed to the projected change in daytime sea breeze convergence showing a larger decrease over western Taiwan than eastern Taiwan. Among the four future runs, the CAR frequency of FC1, which shows an increase in the eastern region of Taiwan, differs from the other runs. This implies some sensitivity of CAR frequency changes in responses to variations in SST, which will be discussed further later.

On the other hand, the increase in CAR intensity is mainly revealed in coastal regions and eastern mountainous regions for most future runs (Fig. 2e). Regarding the CAR amount, all future runs project a decrease along the west side of the mountainous regions but an increase along the east side, particularly in the north east (Fig. 2f). By comparing Fig. 2f with Fig. 2d, e, it is clear that the projected decrease in CAR amount along the west side of the mountainous region is mainly attributed to the decrease in CAR frequency, while the increase in CAR amount over eastern Taiwan is mainly dominated by the changes in CAR intensity rather than the changes in CAR frequency. Further comparison for the sign of changes between CAR amount versus CAR frequency and CAR intensity (Supplementary Fig. 2) demonstrates that changes in CAR frequency play a more important role than CAR intensity over most of the areas with declines in CAR amount, while a reverse situation is true over the areas with increases in CAR amount. Regarding FC1, in which both CAR frequency and intensity increased in the eastern region of Taiwan, it is worth noting that the projected increase in CAR amount over eastern Taiwan is more distinct and substantial compared to the other three runs. Qualitatively, these results indicate that the projected changes (increase or decrease) in CAR amount in Taiwan are more regionally dependent than that of CAR frequency and intensity. Thus, making it more challenging to explain the "sign" changes in the projected future changes in area-averaged CAR amount over Taiwan compared to the respective changes in CAR frequency and CAR intensity (Supplementary Table 3).

It is worth noting that although the four future runs all show projected decreases in CAR frequency and increases in CAR intensity over Taiwan (Fig. 2), there are some differences in the magnitude of changes among the four runs. To better illustrate these differences, we constructed the difference between FC0 and

the other three future runs (FC1, FC2, and FC3) for CAR frequency (Fig. 3a), intensity (Fig. 3b), and amount (Fig. 3c) area-averaged over Taiwan. We selected FC0 as the reference base because the related SST condition represents the ensemble mean of all 28 CMIP5 models (Supplementary Table 1), and also FC0 was commonly used as a single forcing in earlier related studies[13,34]. As shown in Fig. 3a, FC1 projects more CAR frequency than FC0, while FC2 and FC3 project less CAR frequency than FC0 in Taiwan. In contrast to CAR frequency, all FC1 to FC3 runs project lower CAR intensities than those projected by FC0 in Taiwan, where FC2 shows the highest percentage decrease, indicating the least intense CAR among the future runs compared to FC0 (Fig. 3b). In response to these changes in CAR frequency and intensity, FC1 shows a highest, while FC2 shows the smallest CAR amount in Taiwan (Fig. 3c).

In light of these differences in CAR characteristics, two questions are raised: (1) Why does FC1 have more CAR days, while FC2 and FC3 have fewer CAR days? (2) What caused FC2 to have the smallest CAR intensities? Next, we examined possible mechanisms to answer these questions, including a discussion of how SST impacts regional atmospheric thermodynamic changes in the future. Fig. 4 shows the projected changes in SST from the FC0 run compared to the present-day simulation (Pday) (Fig. 4a), and the difference between FC0 and the other three future runs (Fig. 4b–d). It is noted that even though all four runs projected a global increase in SST in the future (Supplementary Fig. 3), the FC1 and FC2 runs show a weaker and a stronger warming pattern, respectively, compared to FC0 over the central to eastern tropical Pacific Ocean region (covering NINO3.4 index region). As a result, the difference between FC1 and FC0 shows a La Niña-like pattern, in contrast to an El Niño-like pattern seen in the difference between FC2 and FC0 (Fig. 4b, c). Conversely, FC3 exhibits a significant increase in SST relative to FC0 over the northern Pacific region (Fig. 4d). These varying degrees of Pacific SST warming patterns might lead to differences in atmospheric thermodynamic conditions, which in turn lead to the differences in CAR characteristics in Taiwan. Evidence for supporting this hypothesis is presented herein.

Possible mechanisms

Huang et al.[19] demonstrated that the CAR frequency in Taiwan during 1960−2012 JJAs was significantly modulated by local thermal instability, local diurnal wind convergence, and the prevailing southwesterly low-level monsoonal flow over the East Asian monsoon region. Building upon these past discoveries, we investigated the projected future changes in these
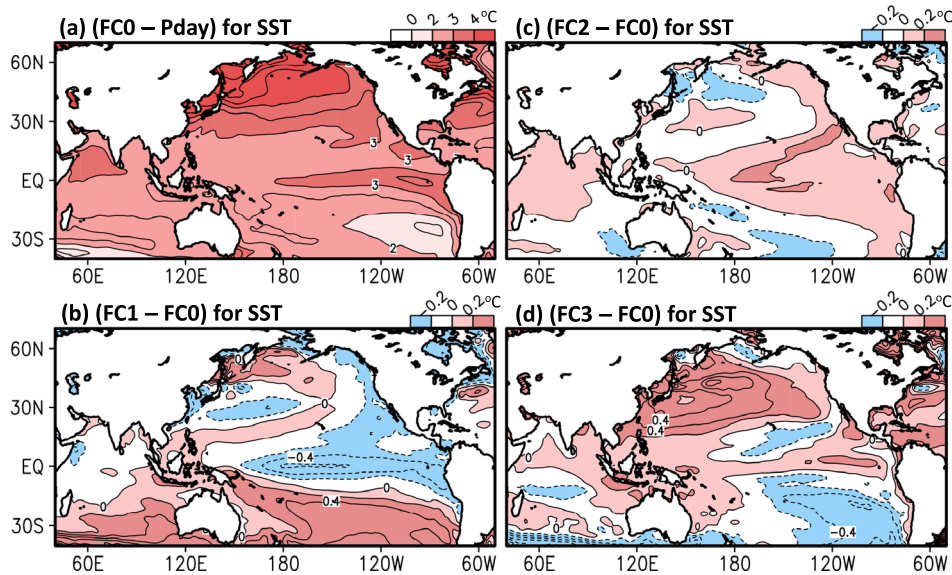
Fig. 4 Future changes in mean sea surface temperature (SST). Projected changes in SST, estimated from: (**a**) differences between the future projection using FC0 run and the present-day simulation (Pday). **b** to (**d**) are for the differences between the future projection using FC0 and the other three future runs (FC1 − FC0, FC2 − FC0, and FC3 − FC0), respectively.
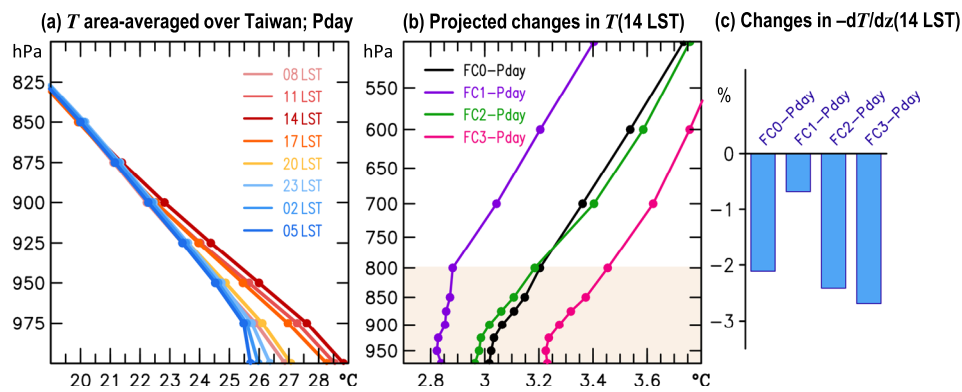
Fig. 5 Thermal condition examinations for explaining CAR frequency change. a Present-day (Pday) vertical distribution of area-averaged temperature (*T*) over Taiwan at different local standard time (LST). **b** Future projected changes (future minus Pday) in area-averaged *T* over Taiwan at 14 LST, estimated from the differences between four future runs (FC0, FC1, FC2, and FC3) and the Pday. **c** The percentage changes in future projected vertical thermal instability (-d*T*/d*z*) (%; see Eq. (3) for the calculation method) estimated from the area-averaged *T* (800 hPa) minus *T* (950 hPa) over Taiwan at 14 LST. The vertical domain between 800 hPa and 950 hPa is shaded in (**b**).

thermodynamic factors and compared these changes across the four future runs to determine if they explain the disparities in CAR frequency. The logical sequence of the analysis and discussion can be summarized as follows: first, the local temperature change was examined, followed by establishing a connection between these changes and regional circulation pattern changes. This linkage was then extended to encompass broader shifts in atmospheric circulation dynamics, finalizing the investigation into how changes in SST will influence the future variations in local CAR in Taiwan.

Fig. 5a shows the vertical profiles of simulated temperature area-averaged over the entire land area of Taiwan at specific times throughout an average day in 1979−2003 JJAs. Notably, the highest temperature over Taiwan at the low-levels occurs at 14 LST. To assess the projected changes in temperature, we constructed the difference between the future and present for the vertical temperature profile area-averaged over Taiwan from the four runs (Fig. 5b), using 14 LST as the reference time step. Overall, the projected changes in all four runs (Fig. 5b) indicate a larger increase in temperature at the upper-levels than lower-levels. Among the runs, FC1 shows the smallest vertical temperature gradient (−d*T*/d*z*), followed by FC0, FC2, and FC3,

showing the values from small to largest, respectively (Fig. 5c). This vertical temperature gradient results suggest that FC1 has a lower thermal stability in comparison to other three runs. Larger thermal stability is generally unfavorable for the formation of local convection, which might lead to a further decrease in CAR frequency[13]. Therefore, the projected changes of a smaller decrease in CAR frequency in FC1 than in other runs (Figs. 2d and 3c) can be reasonably attributed to the projected changes in local thermal stability (Fig. 5b, c). These findings reaffirm that changes in local thermal stability play a crucial role in the projected changes in CAR frequency in Taiwan, consistent with previous studies[13].

Additionally, we examined the projected changes in daytime diurnal wind convergence at 14 LST to understand the changes in local dynamical lifting. The Pday simulation in Fig. 6a demonstrates that Taiwan is under the modulation of sea-breeze convergence at 14 LST, providing dynamical lifting for facilitating convection. All of the projected changes in the four runs suggest that this daytime surface wind convergence feature will be suppressed over Taiwan at the end of the 21st century (Fig. 6b–f). The decrease in surface wind convergence over Taiwan is

unfavorable for CAR formation, resulting in a projected decrease in CAR frequency in the future (Fig. 2d) and reflecting the aforementioned future stable environment. Area-averaged diurnal wind convergence at 14 LST over Taiwan shows that FC1's projection has experienced a smaller decrease compared to the remaining runs (Fig. 6b), inferring that the dynamic lifting in FC1's projection is stronger than in FC0, FC2, and FC3. As a result of both the smallest decline in thermal instability (Fig. 5c) and the daytime dynamical lifting (Fig. 6b), FC1 projects a higher CAR frequency than the other three runs, with a minimum deviation to the Pday.
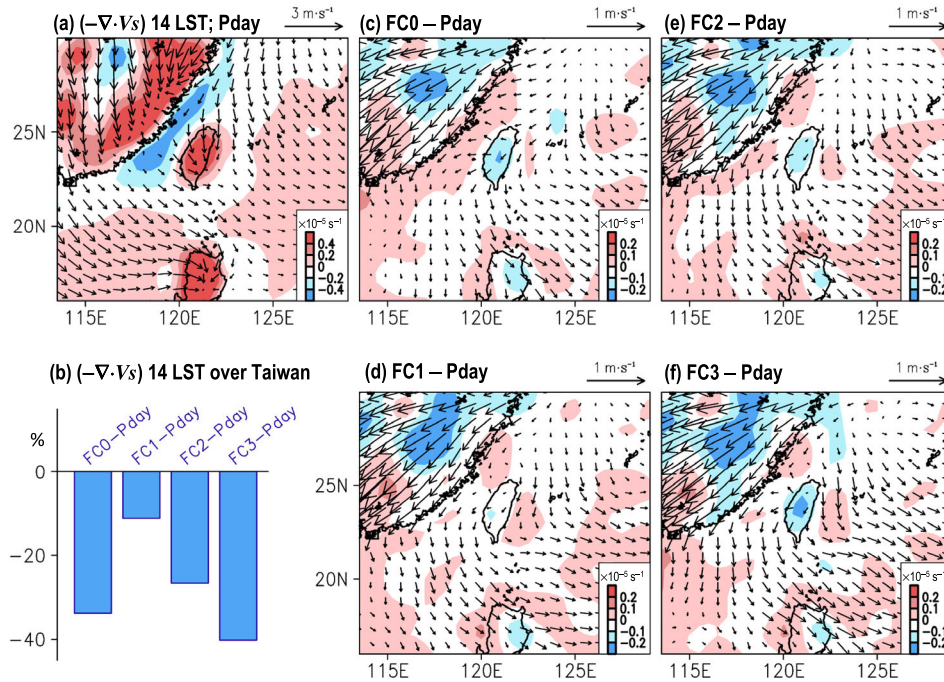
Fig. 6 Dynamical condition examinations for explaining CAR frequency change. a Present-day (Pday) surface wind convergence ($-\nabla \cdot Vs$; shaded) superimposed with the surface wind (vectors) at 14 LST (daily mean removed). **b** The percentage changes in future projected surface wind convergence (%; see Eq. (3) for the calculation method) at 14 LST area averaged over the domain in (**c**–**f**). **c**–**f** are similar to (**a**) but for the future projected changes (future minus Pday) at 14 LST; (**c**) FC0 − Pday, (**d**) FC1 − Pday, (**e**) FC2 − Pday, and (**f**) FC3 − Pday runs.
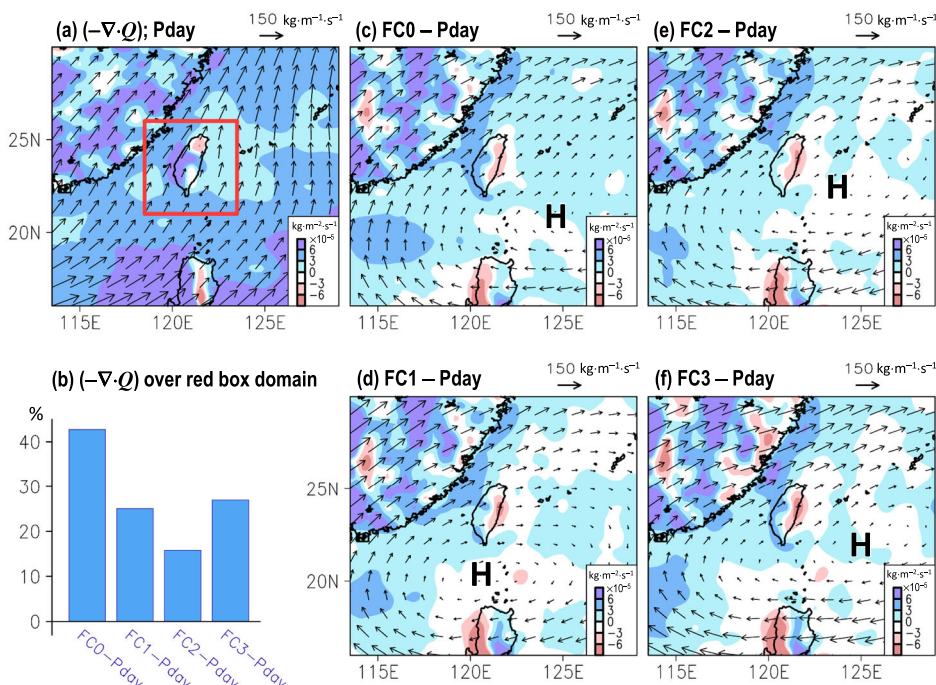
Fig. 7 Moisture flux examinations for explaining CAR intensity change. a Present-day simulation (Pday) of daily mean vertically integrated moisture flux convergence ($-\nabla \cdot Q$, shaded, see Eq. (4) for the calculation method) superimposed with its related vectors. **b** The percentage changes in future projected ($-\nabla \cdot Q$) (%; see Eq. (3) for the calculation method) area-averaged over the red box domain in (**a**). **c**–**f** are similar to (**a**) but for the future projected changes (future minus Pday) at 14 LST; (**c**) FC0 − Pday, (**d**) FC1 − Pday, (**e**) FC2 − Pday, and (**f**) FC3 − Pday runs. Respective anticyclonic centers are marked as "H".
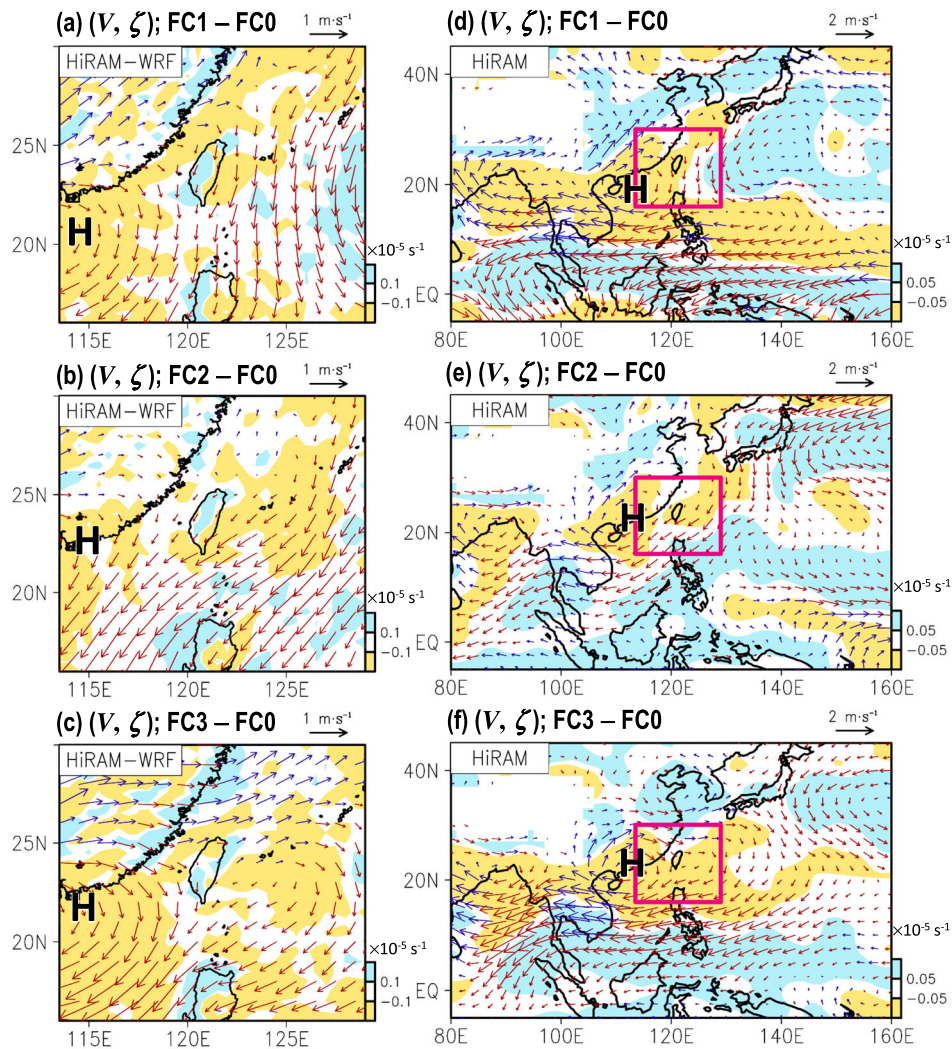
Fig. 8 Connection between local and regional circulation changes. Future simulation differences between the FC0 run and the other three runs for the low-level wind circulation (*V*; vectors) superimposed with vorticity (*ζ*; shaded) at 850 hPa, estimated from HiRAM-WRF: (**a**) FC1 − FC0, (**b**) FC2 − FC0, and (**c**) FC3 − FC0. **d**–**f** are similar to (**a**–**c**) respectively, but for a larger domain where *V* and *ζ* at 850 hPa are extracted from HiRAM future projections. The domain of (**a**–**c**) is marked in a red box in (**d**–**f**). Respective anticyclonic centers are marked as H.

In contrast, FC3 has the largest decline in both thermal instability (Fig. 5c) and daytime dynamical lifting (Fig. 6b), but the difference revealed in both Figs. 5c and 6b between FC0 and FC3 is much smaller than those observed between FC0 and FC1. This also matches well with the difference of CAR frequency shown in Fig. 3a. However, it should be noted that for FC2, its decrease in thermal instability is larger than FC0, but the decrease in dynamical lifting is smaller than FC0. Therefore, the reason that FC2 shows less CAR occurrence frequency than FC0 might be contributed mainly by the difference in the thermal instability rather than the difference in the daytime dynamical lifting between FC0 and FC2. These results underscore the importance of considering thermal instability and dynamic lifting in explaining the projected changes in future CAR frequency over Taiwan.

To establish the connection between local thermodynamic changes and regional circulation changes, we examined the low-level mean circulation from the Pday simulation and the related future projected changes (vectors in Supplementary Fig. 4). The results indicate that Taiwan will experience a modulation of anticyclone circulation, a feature consistent across all four runs, although the anticyclone center location shows some differences among them. Furthermore, we observed that all four runs project a weakening of the monsoon trough, which will lead to a more

stable regional environment resulting in stable thermal stability (Fig. 5) and a decline in dynamical lifting (Fig. 6), in Taiwan in the future. The weakening of the monsoon trough is a part of the results from the enhanced anticyclonic flow over the east of Taiwan. Possible causes for this enhanced anticyclonic flow are found to be related to the SST changes in the eastern tropical Pacific region (discussed later). Analyzing the moisture changes (shaded in Supplementary Fig. 4), we observed that moisture is projected to increase in the future around Taiwan for all four runs, partly contributing to the projected increase in rainfall intensity. However, focusing on the differences among the four runs, we find that FC0 shows the largest increase in moisture while FC1 exhibits the smallest increase (bar in Supplementary Fig. 4). This, however, does not adequately explain why FC2 displays the smallest increase in CAR intensity in Taiwan.

Therefore, we further investigated the vertically integrated moisture flux convergence from the Pday simulation (Fig. 7a) and the related projected changes (Fig. 7b–f). The overall distribution of moisture flux transportation aligns with the low-level circulation seen in Supplementary Fig. 4, showing enhanced anticyclonic flow over the east of Taiwan, indicating a suppression of the monsoonal trough. However, when compared to the analysis based solely on moisture changes (Supplementary Fig. 4), the
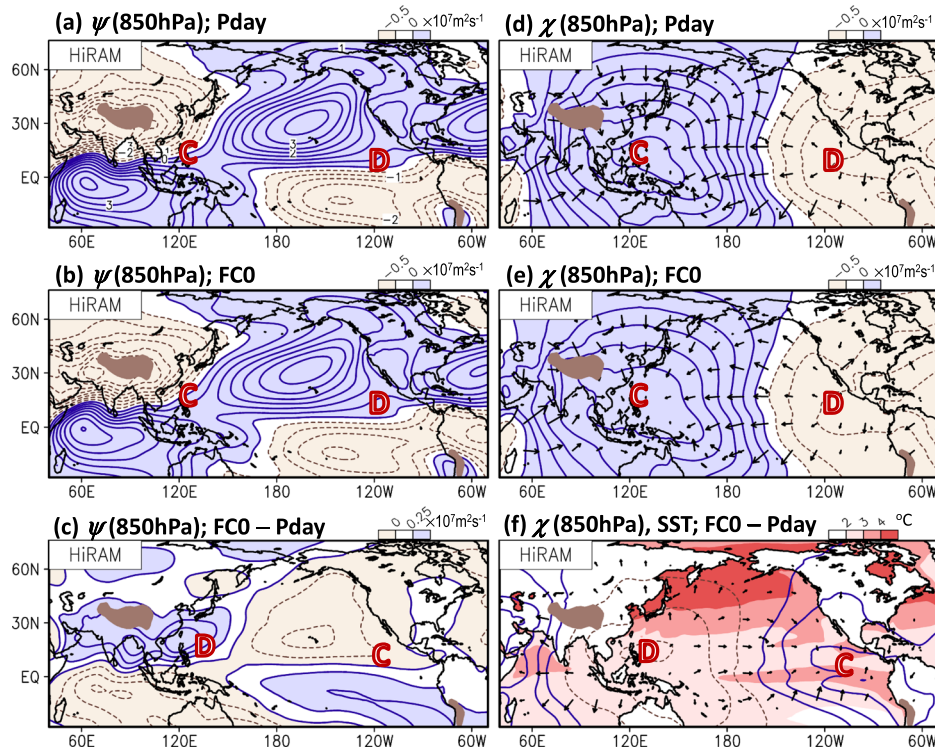
Fig. 9 Present and future simulation of global circulation. Horizontal distribution of streamfunction (ψ) at 850 hPa for (**a**) present-day simulation (Pday), (**b**) future projection using FC0 run, and (**c**) difference between (**b**, **a**) (Future minus Pday). **d**–**f** are similar to (**a**–**c**) respectively, but for the velocity potential function (χ) at 850 hPa. In (**f**), SST difference between the FC0 run and Pday simulation is shaded. Respective convergence (divergence) centers are marked as C (D) in red. All calculations are based on HiRAM data. Topography is marked by brown color.

examination of the vertically integrated moisture flux convergence (Fig. 7b) provides a better representation of the projected changes in CAR intensity. Notably, it reveals the largest convergence in FC0 and the smallest convergence in FC2, leading to the CAR intensity being the most active in FC0 and least active in FC2 (Fig. 3d). These results suggest that the changes in moisture flux transportation play a more crucial role than the changes in local moisture in explaining the projected changes in CAR intensity.

Linkage with SST changes

Notably, the patterns observed in Figs. 5–7 are limited to a small domain, making it challenging to discern the impact of ENSO on these circulation changes. In other words, while the dynamical downscaling simulation provides more detailed information on local and regional features, the domain constraint hinders the assessment of large-scale patterns. To better connect these local and regional features to the large-scale features, we compared the summer mean circulation projected by HiRAM-WRF over a regional domain (Fig. 8a–c) with those projected by the original HiRAM over a larger domain (Fig. 8d–f). Additionally, to better illustrate the relative circulation differences in response to the SST changes shown in Fig. 7c–f, we plotted the future horizontal distribution patterns of vorticity and low-level wind for FC1, FC2, and FC3 by removing the projection using FC0 as shown in Fig. 8. Since spectral nudging was applied to dynamical downscaling, it is reasonable to observe that the circulations in HiRAM-WRF (Fig. 8a–c) are similar to those in HiRAM (Fig. 8d–f). Another noticeable feature in Fig. 8a–c is that FC1, FC2, and FC3 exhibit an enhanced northerly wind component compared to FC0, implying that the projected southwesterly monsoonal flow over the northern South China Sea (see Supplementary Fig. 4) is weaker in FC1, FC2, and FC3 than in FC0. This further implies that the moisture flux

transporting from the northern South China Sea to Taiwan will be smaller in FC1, FC2, and FC3 than in FC0 in the future, partly explaining the features revealed in Fig. 7b.

The larger domain simulated by HiRAM (Fig. 8d–f) further demonstrates that the northerly wind component is part of the enhanced anticyclone in the west of Taiwan, covering the northern South China Sea and South China. The location differences in this subtropical anticyclonic center (marked as H) further lead to the regional differences in circulation over Taiwan. To establish a connection between these circulation patterns and the potential impacts of ENSO, we analyzed a wider range of streamfunction (denoted as ψ) and velocity potential function (denoted as χ) obtained from HiRAM at 850 hPa covering an area from 40°E to 40°W. Overall, the simulations of ψ(850 hPa) from Pday (Fig. 9a) and FC0 (Fig. 9b) exhibit a robust monsoon thermal low over China and a subtropical oceanic high over the north Pacific Ocean, closely resembling the summer mean circulation features from the observational data[35]. However, when FC0 is subtracted from the Pday simulation (Fig. 9c), it highlights a decrease in East Asian monsoonal low together with a decrease in subtropical Pacific high in the future. A similar weakening in the East Asian monsoon pattern is also noted by Hong et al.[36] suggesting the robustness of our results.

Chen[35] examined the maintenance mechanisms of the summer mean stationary waves over the northern hemisphere and suggested that there is a Sverdrup relationship between ψ(850 hPa) and χ(850 hPa), which shows the convergence (divergence) center of χ(850 hPa) marked as C (D) in Fig. 9 is generally located in the western (eastern) boundary of the low-level subtropical oceanic high and the eastern (western) boundary of the monsoon thermal low. This feature is clearly evident in the comparison between Fig. 9a-b and Fig. 9d-e, not only for the Pday simulation but also for the projected changes. By adopting this ψ
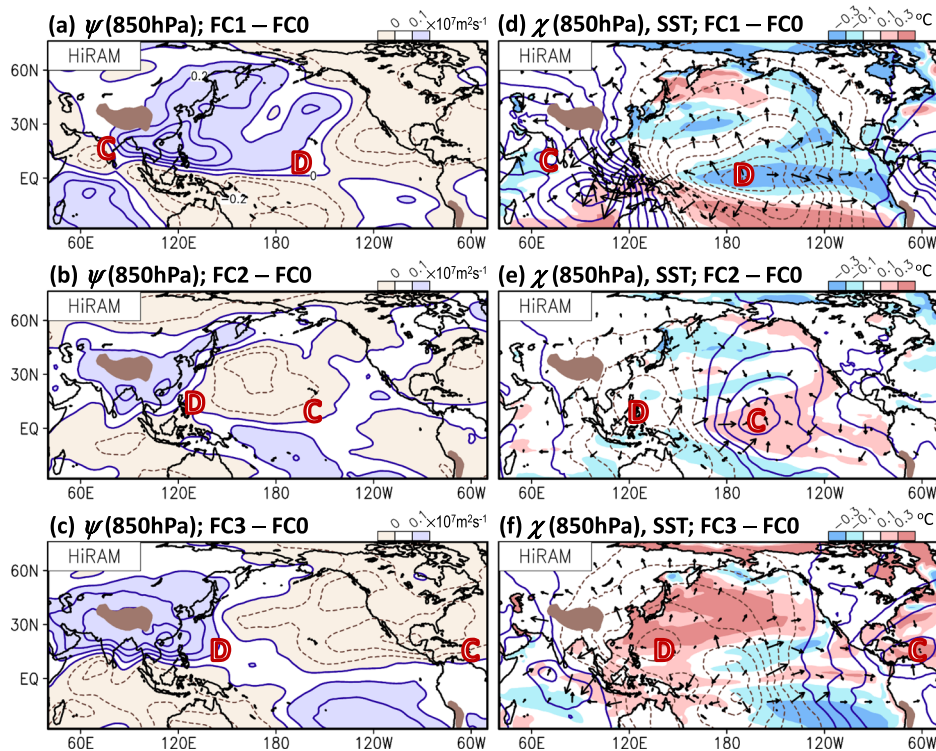
Fig. 10 Future global circulation changes with varying sea surface temperature (SST) patterns. Projected changes in streamfunction (ψ) at 850 hPa (shaded and contoured), estimated between the future projection using FC0 and the other three future runs: (**a**) FC1 − FC0, (**b**) FC2 − FC0, and (**c**) FC3 − FC0. **d–f** are similar to (**a–c**) respectively, but for the velocity potential function (χ) at 850 hPa (contoured) superimposed with the related SST differences (shaded). All calculations are based on HiRAM data. Respective convergence (divergence) centers are marked as C (D) in red. Topography is marked by brown color.

and χ relationship, we can explain the maintenance mechanisms for the projected changes observed in Fig. 9c. Apparently, the enhanced warming of SST over the eastern tropical Pacific (shaded in Fig. 9f) has induced a convergence over there, which further induces a divergence center over the western tropical Pacific (contoured in Fig. 9f) through the east-west walker circulation[37–40]. According to the ψ and χ relationship, this divergence center is part of the maintenance mechanisms for the enhanced anticyclone center (i.e., aforementioned weakening of monsoon trough) that appeared over east of Taiwan.

Fig. 10 represents the ψ(850 hPa) and χ(850 hPa) that are associated with Fig. 9. It is apparent that the tropical SST cold anomaly (i.e., less than average warming) appearing from FC1 minus FC0 has driven a low-level divergence center (marked as D) over the eastern tropical Pacific Ocean (Fig. 10d), which represents a La Niña-like pattern. This divergence center is coupled with a convergence center (marked as C) over 60°−120°E and an anticyclonic system that covers Taiwan is located in-between this east-west dipole of divergence-convergence circulation (Fig. 10a). In contrast, a convergence center over the eastern tropical Pacific driven by the warmer than average SST is revealed by using FC2 minus FC0 (Fig. 10e), which represents an intense El Niño-like pattern. The Sverdrup relationship reveals a cyclonic system over the North Pacific Ocean (Fig. 10b), implying a suppression of subtropical oceanic high over the Pacific Ocean. These ψ and χ relationship aligns with what has been observed in Fig. 9, demonstrating how the differences in SST have driven the changes in χ and the related changes in ψ. Besides, Yu et al.[41] studied the East Asia monsoon transition during the developing El Niño (La Niña) summer, revealing a similar SST anomalies pattern and related circulation response from the perspective of equatorial heating. By comparing Fig. 10 and Fig. 3a, we infer that the La Niña-like circulation pattern can induce more CAR

frequency over Taiwan than the El Niño-like circulation pattern in the future. These results demonstrate that the ENSO has the potential to impact the changes in local CAR occurrence frequency over Taiwan in the future, which is consistent with the observational findings of Huang et al.[17].

Regarding the FC3 minus FC0, we noted from the comparison between Fig. 4a,d that the SST pattern seen in FC3 minus FC0 shows warming mainly over the western north Pacific Ocean, similar to that seen in FC0 minus Pday. As a result, the distribution of ψ(850 hPa) and χ(850 hPa) seen in FC3 minus FC0 (Fig. 10c, f) also shows a similar distribution as those seen in FC0 minus Pday (Fig. 9c, f). The patterns in Fig. 10c, f reflect a stronger suppressed condition over Taiwan in FC3 than in FC0, which not only leads to the fact that FC3 projects a more stable situation over Taiwan than FC0 (e.g., Figs. 5c and 6c) but also makes it more difficult for CAR events to occur in Taiwan in FC3 than in FC0. Huang et al.[17], using observational data from 1960−2012, also noted that the SST changes over the western North Pacific Ocean can impact CAR activities over Taiwan, consistent with the findings for future projection in the current study.

As for the changes in moisture flux transport, we observed from Supplementary Fig. 5 that the global patterns of the convergence/divergence centers for the differences between the future projection using FC0 and the other three future runs (FC1, FC2, FC3) align well with the potential function patterns driven by the SST that shown in Fig. 10d-f. This suggests that changes in SST can lead to changes in the wind circulation, which, in turn, affect the moisture flux transport important to maintaining CAR intensity over Taiwan. As noted in Supplementary Fig. 5, the divergence center of moisture flux is located closer to Taiwan in FC2 than in FC1 and FC3 after removing FC0. This may explain why FC2 exhibits a smaller increase in CAR intensity over Taiwan. This feature, inferred from HiRAM, helps explain why HiRAM-WRF's

simulation of moisture supply around Taiwan is less in FC2 compared to other runs (Fig. 7b).

DISCUSSION

In this study, we investigate the uncertainties surrounding the future projection of CAR activity in Taiwan in response to different sets of future SST changes. The results reaffirmed that HiRAM-WRF has an improved capability in simulating the diurnal rainfall feature in Taiwan compared to HiRAM. Pday simulations using HiRAM-WRF showed that CAR in Taiwan is more frequent and intense over the mountain areas, particularly over the west side. The future runs under different SST boundary conditions all revealed a decrease in CAR frequency but an increased intensity. These changes are attributed to variations in daytime thermal instability, local inland wind convergence, and moisture flux convergence over Taiwan. The study also highlighted the potential impact of ENSO in modulating the changes in CAR activities over Taiwan under global warming, where a La Niña-like circulation patterns induce more CAR activities over Taiwan than El Niño-like circulation patterns. Moreover, results reflect the potential impact of western north Pacific warming in shaping the changes in CAR activities over Taiwan as well.

These findings provide valuable insights into the potential impacts of climate change on CAR events in Taiwan under different SST projection patterns and related mechanisms. Also, this study affirms the influence of ENSO on local CAR, as demonstrated by Huang et al.[17], thereby emphasizing the importance of considering SST changes in projecting future CAR characteristics in Taiwan. Nevertheless, neither Huang et al.[17] nor the current study explains the relative significance of remote or local SST forcing in shaping the changes in CAR characteristics over Taiwan in the future, which deserves further research attention.

METHODS

Model data

All the results presented in this study are obtained from the HiRAM-WRF and HiRAM simulations, with four different SST categories as the boundary forcing (Supplementary Fig. 3). HiRAM is a global model with a horizontal resolution of ~25 km and 32 vertical layers[30]. HiRAM-WRF is the dynamical downscaling of HiRAM, and has a higher resolution of 5 km with 35 vertical layers. For more detailed information about the model setting of HiRAM and HiRAM-WRF, please refer to Zhao et al.[30] and Huang et al.[13], respectively. Regarding the SST forcing, we used the same as Mizuta et al.[20], which classified the SST changes from 28 CMIP5 models into four categories (FC0, FC1, FC2, and FC3). As inferred from the detailed clustering method provided by Mizuta et al.[20] (also outlined in Supplementary Table 2), they employed normalized SST changes (i.e., future minus Pday) to calculate the pattern correlation (requiring re-grid all models to a consistent resolution) prior to the cluster analysis. Also, the classification of SST patterns does not consider the variations in spatial resolution among CMIP5 models, and all models are given equal weight when calculating the averaged SST. Moreover, the SST reproducibility of each of the 28 CMIP5 models is not considered in the cluster analysis because the cluster analysis utilizes the SST changes from future minus Pday, rather than the differences between model and observation.

The Pday simulation covered the JJA of 1979−2003, following Huang et al.[13]. Considering that HiRAM-WRF can simulate diurnal rainfall changes in Taiwan better than HiRAM (Fig. 1), this study focuses on the related results of HiRAM-WRF for the regional rainfall features. Meanwhile, the results of HiRAM can only be used to establish links between local and large-scale features and to explain the potential impact of SST changes on circulation. For the future projection, we used the RCP8.5 scenario[27] with simulations spanning over the JJA from 2075 to 2099, representing the end of the 21st century. Unless otherwise specified, our results of Pday simulation represent the daily average during 1979−2003 JJAs, while the results of future projections represent the daily average during 2075−2099 JJAs.

Identification of CAR features

We adopted definitions from previous studies[13,42] to detect occurrences of CAR events over Taiwan. Initially, a day with a daily rainfall accumulation >0.1 mm was identified as a "rainy day". Next, three criteria were set up to identify CAR days among the identified rainy days as follows: (1) the amount of rainfall accumulated during 01:00–11:00 LST should be <10% of the daily rainfall, (2) the amount of rainfall accumulated during 12:00–22:00 LST should exceed 80% of the daily rainfall, and (3) the rainy pattern should not be influenced by other non-local weather patterns such as typhoons or fronts. The CAR amount was calculated by accumulating the rainfall amount for all CAR days. The CAR intensity is then calculated by dividing the CAR amount by the CAR frequency (i.e., intensity = amount/frequency). For more detailed information on identifying CAR events, please refer to the comprehensive guidelines outlined by Huang & Chen[42] and Huang et al.[13]. To compare with the model results, we obtained observational gridded hourly rainfall data from the Taiwan Climate Change Projection and Information Platform (TCCIP). This observational gridded rainfall data, denoted as OBS, had a horizontal resolution of ~1 km. In order to make a comparison with HiRAM-WRF, all OBS and HiRAM rainfall data were re-gridded into 5 km resolution.

Statistical methods

The following statistical methods were employed to validate the performance of the model simulation. The DRV based on the root-mean-square difference (RMSD) was calculated using hourly rainfall and daily mean rainfall for OBS, HiRAM and HiRAM-WRF using the following Eq. (1).

$$\text{DRV} = \sqrt{\frac{\sum_{i=1}^{N}(\text{Rain}_i - \text{Rain}_{mean})^2}{N}}, \qquad (1)$$

where Rain_i, Rain_{mean} and N denote the hourly rainfall for each sample size, the daily mean of rainfall, and the total sample size, respectively. For validating the model results, we used the difference in DRV between the respective models and OBS (Eq. 2), in which the perfect score of DRV difference is zero.

$$\text{DRV difference} = \text{DRV}_{Model} - \text{DRV}_{Obs}, \qquad (2)$$

For estimating the projected changes, we calculated the relative change between an initial value (Pday simulation) and a subsequent change (future simulation) by expressing this as a percentage using Eq. (3).

$$\text{Projected Change}(\%) = \frac{\text{Future} - \text{Pday}}{\text{Present}} \times 100, \qquad (3)$$

The analysis utilized Eq. (4) to estimate the vertically integrated moisture flux convergence $(-\nabla \cdot Q)$.

$$-\nabla \cdot Q = -\nabla \cdot \left[\frac{1}{g} \int_{300hPa}^{1000hPa} Vq dp \right], \qquad (4)$$

In Eq. (4), g is the acceleration due to gravity, V is the horizontal wind, q is the specific humidity, and p is the pressure, respectively.

DATA AVAILABILITY

CODE AVAILABILITY

The relevant codes utilized in this work are available upon reasonable request from the corresponding author.

REFERENCES

1. Tao, C. et al. Diurnal cycle of precipitation over global monsoon systems in CMIP6 simulations. *Clim. Dyn.* **60**, 3947–3968 (2022).
2. Dai, A. Global precipitation and thunderstorm frequencies. part II: diurnal variations. *J. Clim.* **14**, 1112–1128 (2001).
3. Dirmeyer, P. A. et al. Simulating the diurnal cycle of rainfall in global climate models: resolution versus parameterization. *Clim. Dyn.* **39**, 399–418 (2011).
4. Fang, J. & Du, Y. A global survey of diurnal offshore propagation of rainfall. *Nat. Commun.* **13**, 7437 (2022).
5. Yang, G. Y. & Slingo, J. The diurnal cycle in the tropics. *Mon. Weather Rev.* **129**, 784–801 (2001).
6. Chen, G., Iwasaki, T., Qin, H. & Sha, W. Evaluation of the warm-season diurnal variability over East Asia in recent reanalyses JRA-55, ERA-Interim, NCEP CFSR, and NASA MERRA. *J. Clim.* **27**, 5517–5537 (2014).
7. Chen, G., Lan, R., Zeng, W., Pan, H. & Li, W. Diurnal variations of rainfall in surface and satellite observations at the monsoon coast (South China). *J. Clim.* **31**, 1703–1724 (2018).
8. Dai, A. & Trenberth, K. E. The diurnal cycle and its depiction in the community climate system model. *J. Clim.* **17**, 930–951 (2004).
9. Huang, W.-R., Koralegedara, S. B., Tung, P.-H. & Chiang, T.-Y. Seasonal changes in diurnal rainfall over Sri Lanka and possible mechanisms. *Atmos. Res.* **286**, 106692 (2023).
10. Lee, C.-A., Huang, W.-R., Chang, Y.-H. & Huang, S.-M. Impact of multiple-scale circulation interactions on the spring diurnal precipitation over Luzon. *Sci. Rep.* **11**, 9937 (2021).
11. Sato, T., Miura, H., Satoh, M., Takayabu, Y. N. & Wang, Y. Diurnal cycle of precipitation in the tropics simulated in a global cloud-resolving model. *J. Clim.* **22**, 4809–4826 (2009).
12. Yamamoto, M. K., Furuzawa, F. A., Higuchi, A. & Nakamura, K. Comparison of diurnal variations in precipitation systems observed by TRMM PR, TMI, and VIRS. *J. Clim.* **21**, 4011–4028 (2008).
13. Huang, W.-R. et al. Summer convective afternoon rainfall simulation and projection using WRF driven by global climate model. Part I: over Taiwan. *Terr. Atmos. Ocean Sci.* **27**, 659–671 (2016).
14. Chen, T.-C., Huang, W.-R. & Yen, M.-C. Interannual variation of the late spring–early summer monsoon rainfall in the northern part of the South China Sea. *J. Clim.* **24**, 4295–4313 (2011).
15. Wang, S.-Y. & Chen, T.-C. Measuring East Asian summer monsoon rainfall contributions by different weather systems over Taiwan. *J. Appl. Meteorol. Climatol.* **47**, 2068–2080 (2008).
16. Wang, S.-Y., Chia, H.-H., Gillies, R. R. & Jiang, X. Quasi-biweekly mode and its modulation on the diurnal rainfall in Taiwan forecasted by the CFS. *Weather Forecast.* **28**, 981–993 (2013).
17. Huang, W.-R., Chang, Y.-H. & Huang, P.-H. Relationship between the interannual variations of summer convective afternoon rainfall activity in Taiwan and SSTA(Nino3.4) during 1961-2012: characteristics and mechanisms. *Sci. Rep.* **9**, 9378 (2019).
18. Huang, W.-R., Chang, Y.-H., Deng, L. & Liu, P.-Y. Simulation and projection of summer convective afternoon rainfall activities over Southeast Asia in CMIP6 models. *J. Clim.* **34**, 5001–5016 (2021).
19. Huang, W.-R., Hsu, H. H., Wang, S. Y. & Chen, J. P. Impact of atmospheric changes on the low-frequency variations of convective afternoon rainfall activity over Taiwan. *J. Geophys. Res. Atmos.* **120**, 8743–8758 (2015).
20. Mizuta, R. et al. Classification of CMIP5 future climate responses by the tropical sea surface temperature changes. *Sola* **10**, 167–171 (2014).
21. Huang, W.-R. & Wang, S.-Y. S. Future changes in propagating and non-propagating diurnal rainfall over East Asia. *Clim. Dyn.* **49**, 375–389 (2017).
22. Kusunoki, S., Mizuta, R. & Matsueda, M. Future changes in the East Asian rain band projected by global atmospheric models with 20-km and 60-km grid size. *Clim. Dyn.* **37**, 2481–2493 (2011).
23. Bian, Q. & Lu, R. Impact of sea surface temperature trend on late summer Asian rainfall in the twentieth century. *J. Geophys. Res. Atmos.* **118**, 4256–4266 (2013).
24. Taylor, K. E., Stouffer, R. J. & Meehl, G. A. An overview of CMIP5 and the experiment design. *Bull. Am. Meteorol. Soc.* **93**, 485–498 (2012).
25. Chen, C.-A., Hsu, H.-H., Liang, H.-C., Chiu, P.-G. & Tu, C.-Y. Future change in extreme precipitation in East Asian spring and Mei-yu seasons in two high-resolution AGCMs. *Weather Clim. Extrem.* **35**, 100408 (2022).
26. Chen, C.-A. et al. Seasonal precipitation change in the Western North Pacific and East Asia under global warming in two high-resolution AGCMs. *Clim. Dyn.* **53**, 5583–5605 (2019).
27. Riahi, K. et al. RCP 8.5—A scenario of comparatively high greenhouse gas emissions. *Clim. Change* **109**, 33–57 (2011).
28. Skamarock, W. C. & Klemp, J. B. A time-split nonhydrostatic atmospheric model for weather research and forecasting applications. *J. Comput. Phys.* **227**, 3465–3485 (2008).
29. Skamarock, W. C. et al. *A Description of the Advanced Research WRF Version 3*. NCAR Tech. Note (No. NCAR/TN–475+STR) (University Corporation for Atmospheric Research, 2008).
30. Zhao, M., Held, I. M., Lin, S.-J. & Vecchi, G. A. Simulations of global hurricane climatology, interannual variability, and response to global warming using a 50-km resolution GCM. *J. Clim.* **22**, 6653–6678 (2009).
31. Hassim, M. E. E., Lane, T. P. & Grabowski, W. W. The diurnal cycle of rainfall over New Guinea in convection-permitting WRF simulations. *Atmos. Chem. Phys.* **16**, 161–175 (2016).
32. Kendon, E. J. et al. Heavier summer downpours with climate change revealed by weather forecast resolution model. *Nat. Clim. Change.* **4**, 570–576 (2014).
33. Zhang, Y., Roundy, J. K. & Santanello, J. A. Evaluating the impact of model resolutions and cumulus parameterization on precipitation in NU-WRF: A case study in the central Great Plains. *Environ. Model. Softw.* **145**, 105184 (2021).
34. Huang, W.-R., Chang, Y.-H., Hsu, H.-H., Cheng, C.-T. & Tu, C.-Y. Summer convective afternoon rainfall simulation and projection using WRF driven by global climate model. Part II: over South China and Luzon. *Terr. Atmos. Ocean Sci.* **27**, 673–685 (2016).
35. Chen, T.-C. Characteristics of summer stationary waves in the northern hemisphere. *J. Clim.* **23**, 4489–4507 (2010).
36. Hong, C.-C. et al. Future changes in tropical cyclone intensity and frequency over the western North Pacific based on 20-km HiRAM and MRI models. *J. Clim.* **34**, 2235–2251 (2021).
37. You, Q. et al. Recent frontiers of climate changes in East Asia at global warming of 1.5 °C and 2 °C. *Npj Clim. Atmos. Sci.* **5**, 80 (2022).
38. Yan, Z. et al. Eastward shift and extension of ENSO-induced tropical precipitation anomalies under global warming. *Sci. Adv.* **6**, eaax4177 (2020).
39. Bayr, T., Dommenget, D., Martin, T. & Power, S. B. The eastward shift of the Walker Circulation in response to global warming and its relationship to ENSO variability. *Clim. Dyn.* **43**, 2747–2763 (2014).
40. Ju, J. & Slingo, J. The Asian summer monsoon and ENSO. *Q. J. Roy. Meteorol. Soc.* **121**, 1133–1168 (1995).
41. Yu, T. et al. Roles of ENSO in the link of the East Asian summer monsoon to the ensuing winter monsoon. *J. Geophys. Res. Atmos.* **126**, e2020JD033994 (2021).
42. Huang, W.-R. & Chen, K. C. Trends in pre-summer frontal and diurnal rainfall activities during 1982–2012 over Taiwan and Southeast China: characteristics and possible causes. *Int. J. Climatol.* **35**, 2608–2619 (2015).

AUTHOR CONTRIBUTIONS

W.-R.H. designed the study and led the initial draft. W.-R.H. and Y.-T.C. performed the major analysis. C.-T.C. performed the HiRAM-WRF simulations. All authors discussed the results, read and approved the final manuscript.

COMPETING INTERESTS

The authors declare no competing interests.

ADDITIONAL INFORMATION

Supplementary information The online version contains supplementary material available at https://doi.org/10.1038/s41612-023-00528-7.

Correspondence and requests for materials should be addressed to Wan-Ru Huang.

Reprints and permission information is available at http://www.nature.com/reprints

Publisher's note Springer Nature remains neutral with regard to jurisdictional claims in published maps and institutional affiliations.

Published in partnership with CECCR at King Abdulaziz University